DOI:10.1190/segam2021-3584203.1

Towards practical Bayesian inversion of geobodies using geologic priors

Ashutosh Tewari, Brent Wheelock, Antonio Paiva, Arash Fathi, Myun-Seok Cheon*
ExxonMobil Research & Engineering Company

Summary

We present results on the geophysical inversion of geobodies in a Bayesian framework. Although the methodology applies to all near-homogeneous geobodies, we focus on salt diapirs as they are known to create trapping mechanisms for hydrocarbon reservoirs. Despite a great interest shown by the exploration geophysics community in recent years, the inversion of salt bodies remains a challenge because of severely limited penetration of seismic waves through them, which obscures the view underneath. Hence, with such scarce information in the seismic data, it becomes imperative to quantify uncertainty in inverted salt geometries. *Inverse uncertainty quantification* (a.k.a Bayesian inversion) has a multiyear history in geophysics research. Notwithstanding, the state of the art uncertainty quantification (UQ) methods are simply not practical yet, mainly because a) governing forward models are computationally taxing, and b) the inversion spaces are very high-dimensional owing to the cell-based representation of earth. The crux of this work relies on a low-dimensional representation of salt bodies, which in a Bayesian setting can be viewed as a geologic prior. Equipped with such a prior, we revisit some of the well-known Bayesian methods and reassess their feasibility from a practical standpoint. Specifically, we compare the computational footprint (in terms of number of forward and adjoint solves) of different methods, highlight promising ones, and comment on the future research directions towards practical UQ in geophysical inverse problems.

Introduction

Geophysical inverse problems involve estimating subsurface properties (stratigraphy, rock density, bulk modulus, permeability, porosity etc.) from limited physical measurements (seismic, well logs, well production data etc.). These problems are pervasive in exploration geophysics; a few notable examples from which include seismic travel-time tomography (Phillips, 1991), petrophysical inversion (Alpak, 2006), full waveform inversion (Virieux, 2009; Fathi, 2015, 2016), and reservoir history matching (Rwechungura, 2011) among others. Success of these methods is paramount for many critical business decisions that support acreage acquisition, field exploration, development planning, and reservoir management. A longstanding challenge, common to all geophysical inverse problems is that of ill-posedness, meaning that the physical measurements are hardly informative of the subsurface properties in entirety (Lacasse, 2018). In other words, the inverted subsurface properties remain uncertain since many candidate subsurface models can fit the measurements equally well. Despite this widely-acknowledged fact, the current practice of geophysical inversion, via deterministic optimization techniques, often yields a single subsurface model without any notion of uncertainty in it. State of the art methods to characterize uncertainty in a solution are simply not practical yet, mainly because of a) computationally expensive forward models (Poursartip, 2020), and b) high-dimensional inversion spaces owing to the naïve cell-based representation of earth (Sambridge, 2006). A common thread in recent works in UQ for geophysical inversion is their attempt to reduce the computational cost of exploring the posterior distribution. For instance, dimensionality reduction by using polynomial chaos (Marzouk, 2009), or trans-dimensional parameterization (Ray, 2016, 2019); performing model evaluations with varying levels of fidelity (Peherstorfer, 2016); simultaneous reduced-order model construction and posterior simulation (Cui, 2015); and a Hessian-based MCMC sampling method (Martin, 2012), area a few notable contributions among others.

Recently there is a surge in research efforts (Scheidt, 2018) to develop non cell-based representations of earth, driven by the view that earth is structured (comprising of stratigraphic layers, facies, faults, geobodies etc.), and thus inherently amenable to low-dimensional representations that honor geology in a stricter sense. In a Bayesian setting, such representations can be viewed as geologic priors if they involve a bijective transformation (albeit nonlinear) of a tractable base probability measure (Marzouk, 2016). Some successful applications of such geologic priors for geophysical inverse problems can be found elsewhere (Kadu, 2016, 2017; Tewari, 2019). Here, we focus on the inversion of salt bodies in a media with known properties; a problem that has received considerable attention in exploration geophysics as salt bodies provide excellent seals for hydrocarbon reservoirs. We rely on a parsimonious, parametric representation of salt bodies to yield tractable priors on salt geometry. The thrust of this work is to compare and contrast different Bayesian inference methods in terms of their ability to approximate the true posterior, and their computational requirements in terms of the number of forward and adjoint solves. We limit ourselves to forward models with simplified physics, which greatly speeds up our analysis, while retaining certain characteristics −such as non-linearity and ill-posedness− that make geophysical inverse problems such a big challenge.

Background

Here, we include necessary preliminaries to support the exposition of our work. We first discuss the *shape priors* that play a central role in the Bayesian inversion of salt bodies, followed by a few fundamentally different methods for *posterior approximation* employed in this study.

***Geologic shape prior*:** We design a prior by taking a shape-based parametrization of a discretized inversion domain ($\boldsymbol{\Omega} \in \mathbb{R}^{\boldsymbol{n}}$), wherein $\boldsymbol{\Omega}$ naturally decouples into a subset ($\boldsymbol{\Omega_s} \subset \boldsymbol{\Omega}$) representing a homogenous body with unknown shape, embedded in a known background ($\boldsymbol{\Omega_{bg}} = \boldsymbol{\Omega} \backslash \boldsymbol{\Omega_s}$). Any spatially varying material property m, at an integer location $x \in \{1,2,\cdots,n\}$, can then be represented as

$$m_x = \mathbb{I}_x^s \times m^s + (1 - \mathbb{I}_x^s) \times m^{bg}\,, \qquad (1)$$

where $\mathbb{I}_{\boldsymbol{x}}^{\boldsymbol{s}}$ is the indicator function with value 1 if $x \in \boldsymbol{\Omega_s}$ and 0 otherwise, m^s and m^{bg} are the material property within the shape and outside of it, respectively. A substantive number of works (Aghasi, 2011; Lewis, 2012; Kadu, 2017; Tewari, 2019) have leveraged some form of shape-based parameterization to define $\mathbb{I}_{\boldsymbol{x}}^{\boldsymbol{s}}$. We follow the approach taken in (Tewari, 2019), which represents $\mathbb{I}_{\boldsymbol{x}}^{\boldsymbol{s}}$ as

$$\mathbb{I}_{\boldsymbol{x}}^{\boldsymbol{s}} = \frac{1}{1+\exp\left(-k\left(\boldsymbol{b_x^T\theta} - c\right)\right)}\,, \qquad (2)$$

where the vector $\boldsymbol{b_x} \in \mathbb{R}^p$ is indexed by the location $\boldsymbol{x}$ such that the matrix $\boldsymbol{B} \in \mathbb{R}^{n\times p}$ formed as $\boldsymbol{B} = [\boldsymbol{b_1}\ \boldsymbol{b_2} \cdots \boldsymbol{b_n}]^{\boldsymbol{T}}$ is orthonormal. This representation is motivated by a stochastic viewpoint, which forms a shape by first generating a continuous random field followed by a smooth Heaviside approximation (for instance the sigmoid function in Equation 2). If the random field admits a parsimonious representation (as it does, in this case, via a set of p ($\ll n$) orthonormal basis vector), so does the resulting shapes (c.f. Tewari (2019) for details). In this study $\boldsymbol{p = 60}$ basis vectors are chosen to represent a shape. The scalar c is the level set value that governs the area of the shape (or volume in 3D), and can be set using a-priori knowledge about the subsurface. The scalar k controls the sharpness of the interface between a shape and the background. In the work by Tewari (2019), Equation 2 is used to invert for salt bodies in a full waveform inversion framework, using deterministic optimization techniques. With c fixed and k following a pre-specified annealing schedule, the parameters $\boldsymbol{\theta} \in \mathbb{R}^p$ are optimized using the Gauss-Newton algorithm. It was shown that the low-dimensional salt representation (since $p \ll n$) recovers the complete geometry of a salt body, where traditional cell-based representation could only recover the top of it.

***Bayesian inversion of salt bodies*:** Salt bodies are known to have low density ($\boldsymbol{\rho}$) and high compressional wave velocity ($\boldsymbol{v}$) with respect to the surrounding sedimentary layers in the subsurface. Let, $\boldsymbol{\rho(\theta)} = [\boldsymbol{\rho_1}, \boldsymbol{\rho_2}, \cdots, \boldsymbol{\rho_n}]$ and $\boldsymbol{v(\theta)} = [\boldsymbol{v_1}, \boldsymbol{v_2}, \cdots, \boldsymbol{v_n}]$ be the $\mathbb{R}^p \rightarrow \mathbb{R}_+^n$ mappings defined as per Equations (1) and (2). Assuming access to two types of geophysical measurements viz. gravity ($\boldsymbol{d^g}$) and seismic ($\boldsymbol{d^s}$), described later, our goal is to invert for salt bodies in a Bayesian framework. Equation 3 denotes the log of unnormalized posterior, $\boldsymbol{\tilde{\pi}(\theta)}$, which forms the basis of any Bayesian inference method. The first term is the log-prior of the $\boldsymbol{p}$-dimensional basis coefficients $\boldsymbol{\theta}$. This prior distribution is a zero-mean, isotropic Gaussian (c.f. Tewari (2019) for details). The next two terms are the log-likelihood terms for the two types of measurements in consideration.

$$\log \boldsymbol{\tilde{\pi}(\theta)} = -\frac{\boldsymbol{1}}{\boldsymbol{2}}\boldsymbol{\theta^2} - \frac{\boldsymbol{1}}{\boldsymbol{2(\sigma^g)^2}}\|\boldsymbol{d^g} - \boldsymbol{f^g(\rho(\theta))}\|_{\boldsymbol{2}}^{\boldsymbol{2}} - \frac{\boldsymbol{1}}{\boldsymbol{2(\sigma^s)^2}}\|\boldsymbol{d^s} - \boldsymbol{f^s(\rho(\theta), v(\theta))}\|_{\boldsymbol{2}}^{\boldsymbol{2}} \qquad (3)$$

A typical approach is to assume the residuals (the normed entities in Equation 3) to be independent and identically distributed as a zero-mean, Gaussian with unknown standard deviations (σ^g and σ^s). Here, we set these values by taking into account the length and the variance of the individual measured signals. This allows us to account for any data imbalance as well as differences in the measurement scales between the two measurement types. Because of the non-linearity in the likelihood terms, the normalized posterior of Equation 3 lacks an analytical, closed-form. Hence, we appeal to methods that approximate the posterior distribution as discussed next. Note that the resulting posterior is multimodal, which makes its complete characterization even more challenging (Kaipio, 2005). Nevertheless, in this study we limit our focus on methods that characterize uncertainty around a single mode as, in practice, we often have access to only a few modes because of prohibitively high computational costs.

***Posterior approximation methods*:** These methods deal with a complex posterior by approximating it with a tractable, parametric distribution (e.g. a Gaussian distribution), which can then serve as a surrogate of the true posterior. The simplest of such methods is the *Laplace approximation* (or *inverse covariance method*) (Oliver, 1998), which approximates the posterior around a mode using a Gaussian distribution. A posterior mode, a.k.a *maximum a posteriori* (MAP) solution, is a local optimum of the unnormalized log-posterior (eq. 3), obtained by invoking a deterministic optimization algorithm, i.e. $\boldsymbol{\theta^*} = \boldsymbol{\mathrm{argmax}_\theta}\ (\log \boldsymbol{\tilde{\pi}}\,(\boldsymbol{\theta}))$. Thereafter, $\boldsymbol{\theta^*}$ serves as the mean of the Gaussian approximation, while its covariance is obtained via the second-order truncated Taylor series expansion of $\log \boldsymbol{\tilde{\pi}(\theta)}$, around $\boldsymbol{\theta^*}$. It is easy to show that this covariance matrix is equivalent to the inverse of negative Hessian matrix at $\boldsymbol{\theta^*}$ (MacKay, 2003; Bui-Thanh, 2013). This entire process is straightforward and deterministic but the accuracy of the approximation is limited to the immediate vicinity of $\boldsymbol{\theta^*}$, and can be grossly misleading depending on how non-Gaussian the posterior is in this neighborhood.

Another posterior approximation method is *variational Bayesian inference* (or simply variational inference, VI). VI chooses a distribution from a known parametric family and fits it to the true posterior. However, unlike the Laplace approximation, the fitting process aims to minimize an overall mismatch between the true posterior and the chosen variational distribution, as measured by the *Kullback-Leibler* (KL) divergence (Blei, 2017). Let $q(\boldsymbol{\theta}; \boldsymbol{\phi})$ represent the

10.1190/segam2021-3584203.1

DOI:10.1190/segam2021-3584203.1

chosen variational distribution with tunable parameters $\boldsymbol{\phi}$. VI entails maximizing the following entity, which is also known as the *evidence lower-bound* (ELBO).

$$\max_{\boldsymbol{\phi}} \mathbb{E}_q[\log \tilde{\boldsymbol{\pi}}(\boldsymbol{\theta})] - \mathbb{E}_q[\log q(\boldsymbol{\theta};\boldsymbol{\phi})] \qquad (4)$$

Here, $\mathbb{E}_q$ denotes the expectation with respect to the chosen variational distribution $q(\boldsymbol{\theta};\boldsymbol{\phi})$. The second term encourages $q(\boldsymbol{\theta};\boldsymbol{\phi})$ to have a large spread, whereas the first term constrains it to the regions with high log- unnormalized posterior values. Optimization under this dual-objective makes the VI approximation generally more representative than the Laplace but at a higher computational cost due to the need to compute the expectations through Monte Carlo techniques. Additionally, the choice of variational distribution plays a central role as its flexibility directly impacts the quality of VI approximation of complex (perhaps multimodal) posteriors. Nevertheless, in this study, we choose a multivariate Gaussian as the variational distribution for its simplicity. In the future work section we allude to more expressive distributions that can be employed in the VI framework to approximate complicated posteriors.

The aforementioned approximation methods are benchmarked against the Hamiltonian Monte Carlo algorithm; a MCMC approach that is provably better at posterior approximation but far more computationally demanding (Neal, 2012). We initialize the HMC sampler at the local mode.

Joint inversion of salt bodies

Figure 1 shows a subsurface domain that will serve as a testbed for our analysis (see figure caption for details on sensing configuration). The chosen subsurface model is inspired by the SEG Advanced Modelling (SEAM) data set (Stefani, 2010), though made smaller and restricted to two-dimensions. Also, the water layer has been removed such that reflections are only initiated at salt-background boundaries. The two types of geophysical measurements employed in our analysis are described as follows.

***Gravity*:** The gravity data are generated using the method of Talwani (1959). A Green function for gravitation attraction due to a rectangular prism of uniform density and infinite extent in one horizontal direction (in/out of the page) is computed for each cell of the model (Figure 1). The Green function represents the gravitation anomaly as measured by each receiver. These are concatenated into a matrix, $\boldsymbol{A^g} \in \mathbb{R}^{l \times n}$, one column per cell, and one row per receiver location. Multiplication of $\boldsymbol{A^g}$ by a vector of cell densities produces the gravity data vector, $\boldsymbol{d^g}$, of the anomaly plotted in Figure 1.

***1D Seismic*:** To keep the computational cost of the forward calculations low, the seismic data are generated using a column-wise layered-earth approximation of the model responding to a normally-incident compressional plane wave. Therefore, the response to each column of compressional velocity, $\boldsymbol{v}$, and density, $\boldsymbol{\rho}$, from the model are independently computed using the method of Kennett & Kerry (1979). The seismic data, $\boldsymbol{d^s}$, are non-linearly related to each column of the cell-based model as they contain both primary and multiple reflections of vertically traveling waves. Preparing for gradient based methods, efficient Jacobian calculations ($\boldsymbol{\partial d^s/\partial \rho}$ and $\boldsymbol{\partial d^s/\partial v}$) were developed by analytic differentiation of the recursion formula in Kennett & Kerry.

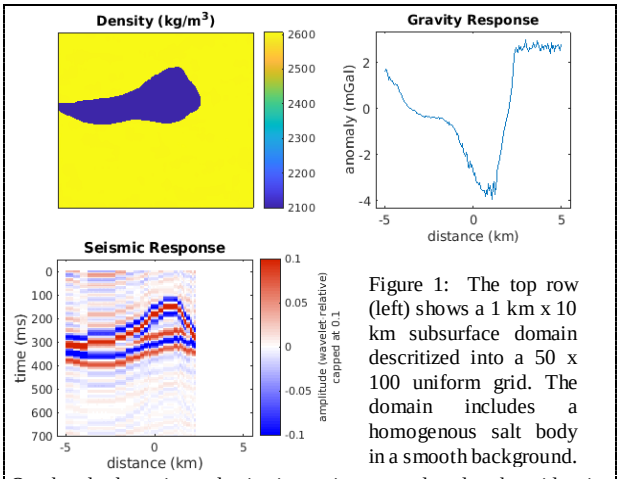

Figure 1: The top row (left) shows a 1 km x 10 km subsurface domain descritized into a 50 x 100 uniform grid. The domain includes a homogenous salt body in a smooth background. One hundred gravity and seismic receivers are placed at the mid-point of each cell in the top row of the model at a depth of 10 meters. The top row (right) and the bottom row (left) show the gravity and seismic response from the respective sensors. The subsequent results use this data to invert for the salt body in a Bayesian setting.

Figure 2 shows an inverted subsurface model, as well as the residual seismic and gravity responses. Note that the inverted model is a local MAP solution (or a mode) of the log unnormalized posterior, $\tilde{\pi}(\theta)$. Another initialization would result in a different mode (perhaps better), since $\tilde{\pi}(\theta)$ is non-concave with multiple local maxima. For now, we limit our focus on quantifying uncertainty around a single mode such as the one shown in figure 2. This mode is chosen because it presents an interesting scenario where the inverted subsurface model suggests the presence of three geobodies in the domain. Since the ground truth is known, we can affirm that the two geobodies (out of three) are inversion artifacts resulting from being stuck at a locally optimal solution. The quantification of uncertainty around this mode, hence, provides valuable information as discussed next.

We first compare the performance of the three posterior approximation methods viz. Laplace, VI and HMC. Figure 3 (left) plots the distribution of the total salt fraction in the whole domain as determined using 2000 independent

DOI:10.1190/segam2021-3584203.1

samples from the three methods. Evidently, HMC characterizes the salt fraction most accurately, while Laplace being the least accurate. This observation is corroborated by comparing the metric ELBO (right plot), which suggests the same descending order in the quality of posterior approximation (HMC→ VI → Laplace). However, this order reverses in terms of computational costs involved in obtaining 2000 independent samples from each of these methods (Table 1 lists the number of forward and adjoint solves invoked by the three methods).

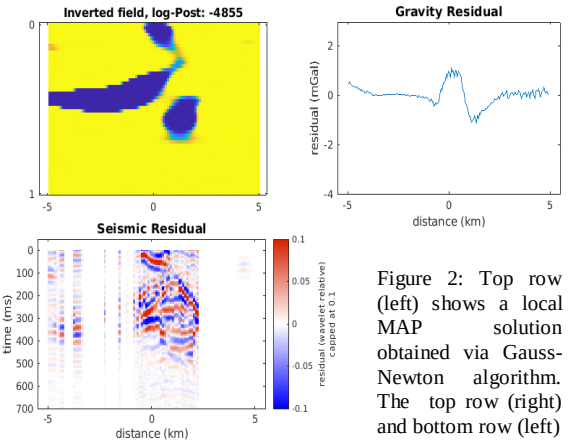

Figure 2: Top row (left) shows a local MAP solution obtained via Gauss-Newton algorithm. The top row (right) and bottom row (left) show the residual gravity and seismic responses plotted using the same scale as Figure 1.

In the last set of results, we identify three zones in the MAP solution with a salt body in each zone (refer to Figure 4). Presence of salt in zones 1 and 2 is an inversion artifact as mentioned earlier. We quantify the uncertainty in salt fraction in these zones using the Laplace, VI, and HMC methods. The same 2000 samples (used in Figure 3) are leveraged for this purpose. The results shown in Figure 4 again suggests inferior posterior approximation by Laplace and VI compared to HMC. The former two suggest a significant salt fractions in zones 1 and 2, when there exists none/small in reality. Note that VI has a marginally better performance than Laplace as indicated by the shift (to the left) in the salt fraction distributions in zone 1. HMC, interestingly, is able to escape the local mode and sample from a region closer to the ground truth.

Conclusion and Future work

We investigate a few well-known, but fundamentally different, Bayesian inference methods for the inversion of homogeneous geobodies using gravity and seismic data in a synthetic setting. The goal is to assess the ability of posterior approximation as well as the computational requirements of these methods. We limit ourselves to posterior approximation around a local MAP solution, in spite of the posterior being a multimodal distribution. Hamiltonian

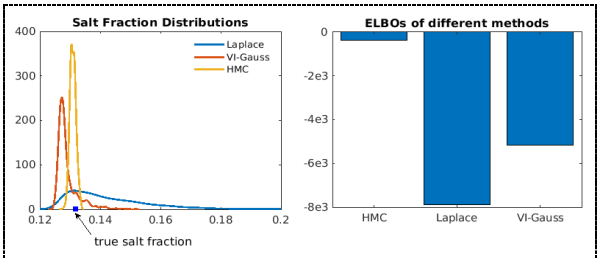

Figure 3: (Left) the distribution of salt fraction, in the whole domain, obtained via the three posterior approximation methods. (Right) comparison of the ELBO values of attained by the three methods. A higher ELBO value indicates better posterior approximation.

Table 1: Comparison of the number of forward and adjoint solves invoked by the three methods to obtain 2000 independent samples.

	# forward solves	# adjoint solves
Laplace	60	60
VI-Gauss	3,300	1,500
HMC	150,000	150,000

Monte Carlo (HMC), understandably, approximates the posterior the best but at a very high computational cost. Overall, the variational inference (VI) framework seems to provide an attractive alternative to HMC, provided one can utilize a flexible family of distributions to approximate the posterior. Recent works on VI using *optimal transport maps* (Marzouk, 2016) and *normalizing flows* (Rezende, 2015) look promising to enable practical UQ in geophysical inverse problems, and thus, form the focus of our future research. Another line of research would be to develop adjoint-free VI methods that rely solely on forward solves of varying fidelity and precision in an attempt to relax computer memory requirements. These accommodations are particularly attractive for emerging computing platforms, which have the potential to significantly speed up PDE-based simulators (Keyes, 2020).

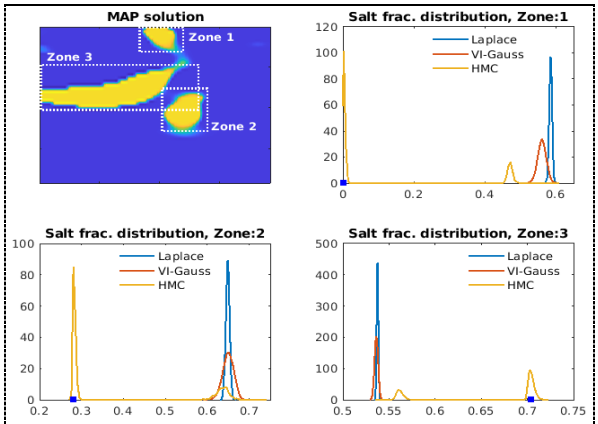

Figure 4: Comparison of salt fraction distributions, obtained by the three methods, in three zones shown in the top-left plot. Each zone represents a region of the subsurface with a contiguous salt body. The plotted salt fraction densities are obtained by 2000 independent samples from the three posterior approximation methods. The blue markers represent ground truth.

REFERENCES

Aghasi, A., M. Kilmer, and E. L. Miller, 2011, Parametric level set methods for inverse problems: SIAM Journal on Imaging Sciences, **4**, 618–650, doi: https://doi.org/10.1137/100800208.

Alpak, F. O., C. Torres-Verdín, and T. M. Habashy, 2006, Petrophysical inversion of borehole array-induction logs: Part I — Numerical examples: Geophysics, **71**, no. 4, F101–F119, doi: https://doi.org/10.1190/1.2213358.

Bui-Thanh, T., O. Ghattas, J. Martin, and G. Stadler, 2013, A computational framework for infinite-dimensional Bayesian inverse problems part I: The linearized case, with application to global seismic inversion: SIAM Journal on Scientific Computing, **35**, A2494–A2523, doi: https://doi.org/10.1137/12089586X.

Blei, D. M., A. Kucukelbir, and J. D. McAuliffe, 2017, Variational inference: A review for statisticians: Journal of the American Statistical Association, **112**, 859–877, doi: https://doi.org/10.1080/01621459.2017.1285773.

Chen, P., and O. Ghattas, 2019, Hessian-based sampling for high-dimensional model reduction: International Journal for Uncertainty Quantification, **9**, 103–121, doi: https://doi.org/10.1615/Int.J.UncertaintyQuantification.2019028753.

Cui, T., Y. Marzouk, and K. Willcox, 2015, Data-driven model reduction for the Bayesian solution of inverse problems: International Journal for Numerical Methods in Engineering, **102**, 966–990, doi: https://doi.org/10.1002/nme.4748.

Fathi, A., B. Poursartip, K. H. Stokoe, and L. F. Kallivokas, 2016, Three-dimensional P- and S-wave velocity profiling of geotechnical sites using full-waveform inversion driven by field data: Soil Dynamics and Earthquake Engineering, **87**, 63–81, doi: https://doi.org/10.1016/j.soildyn.2016.04.010.

Fathi, A., B. Poursartip, and L. F. Kallivokas, 2015, Full-waveform inversion in three-dimensional PML-truncated elastic media: Computer Methods in Applied Mechanics and Engineering, **296**, 39–72, doi: https://doi.org/10.1016/j.cma.2015.07.008.

Kadu, A., T. Van Leeuwen, and W. A. Mulder, 2016, A parametric level-set approach for seismic full-waveform inversion: 86th Annual International Meeting, SEG, Expanded Abstracts, 1146–1150, doi: https://doi.org/10.1190/segam2016-13870276.1.

Kadu, A., T. Van Leeuwen, and W. A. Mulder, 2017, Salt reconstruction in full-waveform inversion with a parametric level-set method: IEEE Transactions on Computational Imaging, **3**, 305–315, doi: https://doi.org/10.1109/TCI.2016.2640761.

Kaipio, J., and E. Somersalo, 2005, Statistical and computational inverse problems: Springer-Verlag.

Kennett, B., and N. J. Kerry, 1979, Seismic waves in a stratified half space: Geophysical Journal International, **57**, 557–583, doi: https://doi.org/10.1111/j.1365-246X.1979.tb06779.x.

Keyes, D. E., H. Ltaief, and G. Turkiyyah, 2020, Hierarchical algorithms on hierarchical architectures: Philosophical Transactions of the Royal Society A: Mathematical, Physical and Engineering Sciences, **378**, 20190055, doi: https://doi.org/10.1098/rsta.2019.0055.

Lacasse, M. D., L. White, H. Denli, and L. Qiu, 2018, Full-wavefield inversion: An extreme-scale PDE-constrained optimization problem, Frontiers in PDE-Constrained Optimization: Springer, 205–255.

Lewis, W., B. Starr, and D. Vigh, 2012, A level-set approach to salt geometry inversion in full waveform inversion: 82nd Annual International Meeting, SEG, Expanded Abstracts, 1–4, doi: https://doi.org/10.1190/segam2012-0737.1.

MacKay, C. J., 2003, Information theory, inference and learning algorithms: Cambridge university press.

Marzouk, Y., and H. Najm, 2009, Dimensionality reduction and polynomial chaos acceleration of Bayesian inference: Journal of Computational Physics, **228**, 1862–1902, doi: https://doi.org/10.1016/j.jcp.2008.11.024.

Marzouk, Y., T. Moselhy, M. Parno, and A. Spantini, 2016, Sampling via measure transport: An introduction, in Ghanem, R., Higdon, D., and Owhadi, H., eds., Handbook of Uncertainty Quantification: Springer.

Neal, R. M., 2012, Chapter 5: MCMC Using Hamiltonian dynamics, in Handbook of Markov Chain Monte Carlo: CRC Press.

Peherstorfer, B., T. Cui, Y. Marzouk, and K. Willcox, 2016, Multifidelity importance sampling: Computer Methods in Applied Mechanics and Engineering, **300**, 490–509, doi: https://doi.org/10.1016/j.cma.2015.12.002.

Poursartip, B., A. Fathi, and J. L. Tassoulas, 2020, Large-scale simulation of seismic wave motion: A review: Soil Dynamics and Earthquake Engineering, **129**, 105909, doi: https://doi.org/10.1016/j.soildyn.2019.105909.

Phillips, W. S., and M. C. Fehler, 1991, Traveltime tomography: A comparison of popular methods, Geophysics, **56**, 1639–1649, doi: https://doi.org/10.1190/1.1442974.

Ray, A., and D. Myer, 2019, Bayesian geophysical inversion with trans-dimensional Gaussian process machine learning: Geophysical Journal International, **217**, 1706–1726, doi: https://doi.org/10.1093/gjihttps://doi.org//ggz111.

Ray, A., A. Sekar, G. M. Hoversten, and U. Albertin, 2016, Frequency domain full waveform elastic inversion of marine seismic data from the Alba field using a Bayesian trans-dimensional algorithm: Geophysical Journal International, **205**, 915–937, doi: https://doi.org/10.1093/gjihttps://doi.org//ggw061.

Rezende, D. J., and S. Mohamed, 2015, Variational inference using normalizing flows: Proceedings of the 32nd International Conference on International Conference on Machine Learning, **37**, 1530–1538.

Rwechungura, R. W., M. Dadashpour, and J. Kleppe, 2011, Advanced history matching techniques reviewed: Society of Petroleum Engineers Middle East Oil and Gas Show and Conference, SPE, 142497.

Sambridge, M., K. Gallagher, A. Jackson, and P. Rickwood, 2006, Trans-dimensional inverse problems, model comparison and the evidence: Geophysical Journal International, **167**, 528–542, doi: https://doi.org/10.1111/j.1365-246X.2006.03155.x.

Scheidt, C., L. Li, and J. Caers, 2018, Quantifying uncertainty in subsurface systems: American Geophysical Union.

Stefani, J., M. Frenkel, N. Bundalo, R. Day, and M. Fehler, 2010, SEAM update: Models for EM and gravity simulations: The Leading Edge, **29**, 132–135, doi: https://doi.org/10.1190/tle29020132.1.

Talwani, M., J. L. Worzel, and M. Landisman, 1959, Rapid gravity computations for two dimensional bodies with application to the Mendocino submarine fracture zone: Journal of Geophysics Research, **64**, 49–59, doi: https://doi.org/10.1029/JZ064i001p00049.

Tewari, A., and D. Trenev, 2019, An ultra-low-dimensional inversion of homogeneous geobodies in full waveform inversion: 89th Annual International Meeting, SEG, Expanded Abstracts, 1690–1694, doi: https://doi.org/10.1190/segam2019-3216897.1.

Virieux, J., and S. Operto, 2009, An overview of full-waveform inversion in exploration geophysics: Geophysics, **74**, no. 6, WCC1–WCC26, doi: https://doi.org/10.1190/1.3238367.